Supplementary Information 1: Multi-sensor geophysical observations resolve lahar dynamics remotely at Volcán de Fuego, Guatemala

Duccio Gheri[1,*], Silvio de Angelis[1], Rob Duller[1],
Mark Woodhouse[2], Jeremy Phillips[2], Armando Pineda[3],
Amilcar Roca[4] and Roberto Mérida[4]

[1] School of Environmental Sciences, University of Liverpool, 4 Brownlow Street, Liverpool, L69 3GP, UK
[2] School of Earth Sciences, University of Bristol, Queens Road, Bristol, BS8 1RJ, UK
[3] Unaffiliated, Guatemala City, Guatemala
[4] Instituto Nacional de Sismología, Vulcanología, Meteorología e Hidrología (INSIVUMEH), Guatemala City, Guatemala
*Correspondence: d.gheri@liverpool.ac.uk

Supplementary Note: Visual documentation of lahar dynamics

Time-synchronised visual observations of the 15 October lahar are archived in a Zenodo repository [1] and described in the associated Data Descriptor [2]. Here, selected frames are used to illustrate the passage of the lahar through the upper and lower reaches of the instrumented section of the Ceniza channel.

In the upper reach, a high-resolution DJI Osmo 5 Pro camera was installed near station FGL4. The footage captures arrival of the lahar front at 15:35:11 local time (Supplementary Fig. S1a) and the subsequent evolution of the flow. During the initial phase, coarse clasts ranging from decimetre-to-metre scale are visibly mobilised and transported within the flow (Supplementary Fig. S1b). For scale, the wetted channel width is approximately 15 m. Individual boulders are observed rolling and rotating along the channel bed, indicating sustained grain–bed interactions.

In the lower reach, a Brinno time-lapse camera co-located with station FGL8 documents the downstream evolution of the flow (Supplementary Fig. S1c–e). Prior to the lahar arrival, the channel shows relatively low stage and limited visible sediment transport (15:35; Supplementary Fig. S1c). A progressive increase in flow stage is visible at 16:12 (Supplementary Fig. S1d), coincident with the interval of low-amplitude seismic signal in the downstream record. Later images at 17:13 (Supplementary Fig. S1e) show a further increase in flow stage and discharge during the stronger downstream phase of the event, corresponding to the pronounced increase in seismic amplitude and RMSA that culminates in the main downstream pulse.

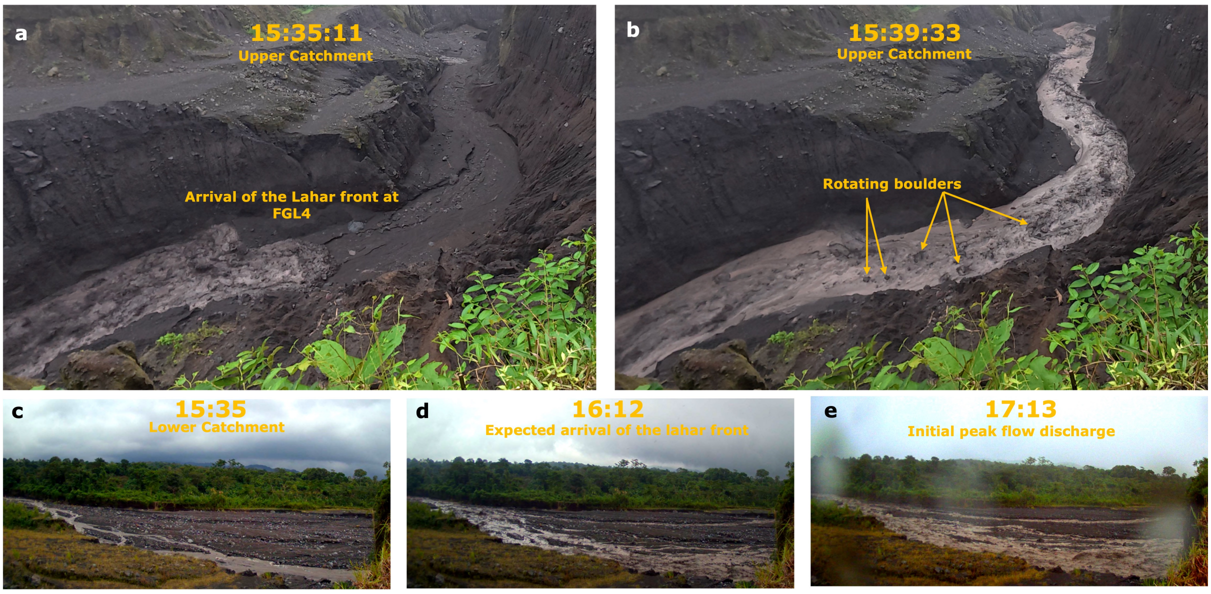

Supplementary Fig. S1: **Visual documentation of lahar dynamics in the Ceniza channel.** **a**, Snapshot from the DJI Osmo 5 Pro camera installed near station FGL4, showing arrival of the lahar front at 15:35:11. **b**, Subsequent phase of the flow (15:39:33), with coarse clasts visible within the flow and along the channel bed. **c–e**, Time-lapse images from the Brinno camera co-located with station FGL8 in the lower reach. **c**, Channel conditions prior to lahar arrival (15:35), showing relatively low stage and limited visible sediment transport. **d**, Progressive increase in flow stage at 16:12, coincident with the interval of low-amplitude seismic signal in the downstream record. **e**, Further increase in flow stage and discharge at 17:13 during the stronger downstream phase of the event, preceding the main downstream seismic pulse. Times are expressed in local time (UTC–6).

Supplementary Methods

Channel morphology analysis

Channel morphology along the instrumented section of the Ceniza channel was quantified using a high-resolution digital elevation model (DEM) and orthomosaic derived from a pre-event drone survey and processed in Agisoft Metashape Professional (Supplementary Fig. S2), following UAV-based mapping approaches previously applied at Fuego [3]. Drone imagery was processed using a Structure-from-Motion workflow that included image-quality screening, photo alignment, iterative camera optimisation, and dense-cloud filtering prior to generation of the final topographic products. DEMs and orthomosaics were produced from the filtered dense cloud in local coordinates and used primarily for relative topographic and geomorphic measurements. Slope angle is shown directly on the DEM for the upper and lower reaches in Supplementary Fig. S2a,b.

A channel centre-line was manually extracted by following the lowest topographic path along the channel bed. The longitudinal elevation profile was then obtained by sampling DEM elevations along this centre-line. Mean channel slopes for the upper and lower reaches were estimated by linear regression of the corresponding segments of the profile (Supplementary Fig. S2c).

Channel width was estimated from cross-channel profiles extracted perpendicular to the centreline at regular intervals. For each profile, the channel boundaries were defined relative to the local minimum elevation. In the upper reach, channel width was measured at 2 m above the minimum elevation of each cross-section, whereas in the lower reach a threshold of 0.5 m was used, reflecting differences in incision depth and cross-sectional morphology between the two reaches. The distance between the two intersection points defines the active channel width.

Width measurements were interpolated along the centre-line to obtain a continuous representation of channel width (Supplementary Fig. S2c). Reach-averaged values were then calculated to derive the representative channel widths and mean slopes used in the main analysis.

Video-based velocity estimation (RIVeR)

Mean surface flow velocity was estimated from video recordings using the RIVeR (Rectification of Image Velocity Results) toolbox [4]. Video data were acquired with a DJI Osmo 5 Pro camera (4K resolution, 25 fps) installed on a stable boulder overlooking the channel (Supplementary Fig. S3a). Timestamps were synchronised via Network Time Protocol (NTP) to ensure consistency with the seismic and infrasonic records.

The video sequence corresponding to lahar passage was trimmed and geometrically calibrated. Spatial calibration was performed using fixed reference points visible in the footage, whose coordinates were obtained from the pre-event drone-derived orthomosaic and digital surface model described above. Stable features such as boulders and channel margins were used to define the image-to-ground transformation.

Velocity estimation was performed within a straight channel reach using the particle image velocimetry (PIV) and particle tracking velocimetry (PTV) routines implemented in RIVeR, which track coherent surface patterns between consecutive frames [4]. The sediment-laden surface provided sufficient natural tracers for robust velocity retrieval. For each time step, the mean surface velocity within the region of interest (ROI) was used in the analysis.

Flow depth was constrained from video observations and cross-sectional geometry derived from the drone survey. During the analysed interval, tested depths ranged between 1.4 and 2.6 m. To assess sensitivity to this parameter, velocity time series were recomputed using representative depths of 1.40, 1.67, 2.26, and 2.61 m over the first 20 s of sustained flow (Supplementary Fig. S3c).

Variations in assumed depth produced systematic but limited changes in velocity magnitude, with differences of less than 0.5 m s^{-1}, while the temporal evolution and peak structure remained unchanged. A depth of 1.40 m was adopted for the main analysis, as it is consistent with the observed flow stage and yields velocity estimates comparable to the independent seismic constraints.

Estimation of the seismic coupling term and sensitivity analysis

Estimation of the seismic coupling term $g(r_0)$

The source–receiver coupling term $g(r_0)$ accounts for seismic coupling, geometrical spreading, intrinsic attenuation, and near-surface wave propagation between the impact zone and the seismic station. Following the physically based formulations of Tsai et al.[5] and Farin et al.[6], $g(r_0)$ was computed in the frequency domain as

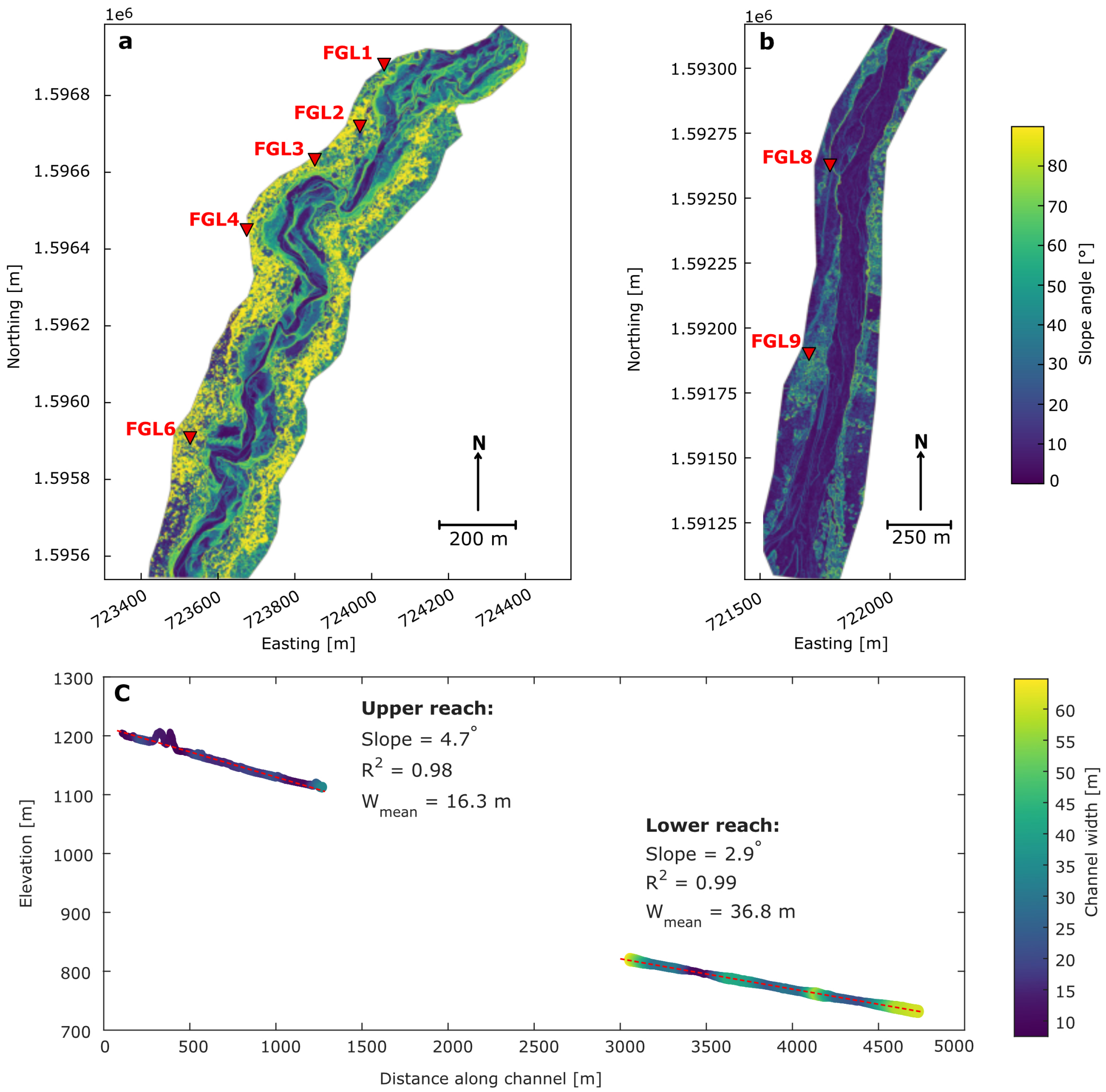

Supplementary Fig. S2: **Channel morphology of the upper and lower reaches of the Ceniza channel.** **a**, Slope-angle map derived from the DEM for the upper instrumented reach (FGL1–FGL6). Geophone locations are indicated by red triangles. Scale bar, 200 m. **b**, Slope-angle map derived from the DEM for the lower reach (FGL8–FGL9). Geophone locations are indicated by red triangles. Scale bar, 250 m. **c**, Longitudinal elevation profile along the extracted channel centreline. Colour indicates channel width (m) derived from cross-channel profiles. Red dashed lines show linear regressions fitted to the upper and lower reaches, used to estimate mean channel slopes. Reach-averaged slope, correlation coefficient, and mean channel width are indicated for each reach.

$$g(r_0) = \frac{\pi^4}{144}\, N_{jz}^2 f_j^2 \left(\frac{\rho_s}{\rho_0}\right)^2 \int_{f_{\min}}^{f_{\max}} \frac{f^3\, \chi(r_0, f)}{v_c(f)^3\, v_u(f)^2}\, df, \tag{1}$$

where ρ_s and ρ_0 are the sediment and ground densities, respectively, $v_c(f)$ and $v_u(f)$ are the frequency-dependent Rayleigh-wave phase and group velocities, and $\chi(r_0, f)$ describes

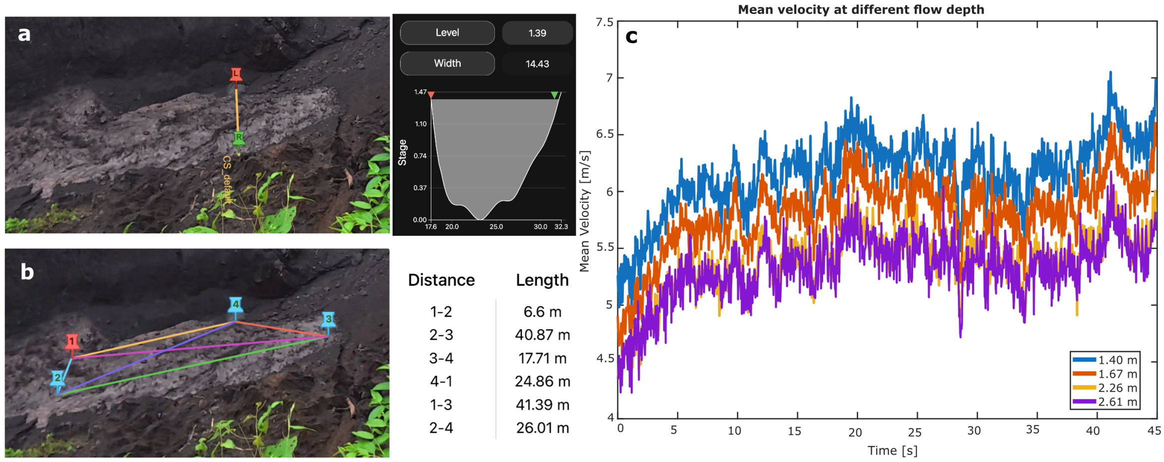

Supplementary Fig. S3: **Sensitivity of RIVeR-derived surface velocity to assumed flow depth.** **a**, Video frame used for geometric calibration and definition of control points. **b**, Planimetric distances between control points used for image rectification. **c**, Mean surface velocity time series within the region of interest (ROI) over the first 20 s of sustained flow, computed for four assumed flow depths (1.40, 1.67, 2.26, and 2.61 m). Increasing depth reduces velocity magnitude, but differences remain below 0.5 m s^{-1} and do not affect temporal patterns or peak timing.

distance-dependent attenuation. Here, N_{jz} denotes the dimensionless coefficient of the surface-wave Green's function controlling the relative amplitude of vertical ground motion generated by a force in direction j, whereas f_j is a dimensionless function describing the characteristic basal impact impulse as a function of the ratio between fluctuating and mean particle velocities [6]. The combined factor $N_{jz}^2 f_j^2$ was set to 0.14 for the thin-flow regime and is included within $g(r_0)$.

Seismic velocities were described using the dispersive power-law relation of Tsai et al.[5],

$$v_c(f) = v_{c0}\left(\frac{f}{f_0}\right)^{-\xi}, \tag{2}$$

with $f_0 = 1$ Hz. The corresponding group velocity was computed as

$$v_u(f) = \frac{v_c(f)}{1+\xi}. \tag{3}$$

Distance-dependent attenuation was computed using the infinite straight-channel approximation,

$$\chi(r_0, f) = 2\,K_0\left(\frac{2\pi f r_0}{v_u(f)\,Q}\right), \tag{4}$$

where K_0 is the modified Bessel function of the second kind and Q is the seismic quality factor.

The integral was evaluated numerically over the same frequency band used for the observed integrated PSD, 1–80 Hz, on a logarithmic frequency grid. This ensures that the coupling term and the observed seismic power refer to the same high-frequency band used in the inversion.

Model parameters were set to $v_{c0} = 800$ m s^{-1}, $\xi = 0.374$, $Q = 5$, and $\rho_s = \rho_0 = 2500$ kg m^{-3}. The reference velocity reflects the expected low near-surface seismic velocities of weakly consolidated volcaniclastic channel material [7–9]. The resulting $g(r_0)$ decreases monotonically with source–receiver distance and was used directly in the thin-flow inversion.

Sensitivity analysis of the seismic inversion

We evaluated the sensitivity of the thin-flow seismic inversion to uncertainties in seismic attenuation and the velocity model (Supplementary Fig. S4). This test is important because near-surface seismic velocity and attenuation can vary substantially in weakly consolidated volcanic debris-flow channels. Recent active-source measurements [10] in the Tahoma Creek debris-flow channel at Mount Rainier showed low Rayleigh-wave velocities, strong attenuation and Q values below 13.3 across the analysed frequency range, and demonstrated that reasonable variations in velocity and attenuation can alter modeled debris-flow spectra by orders of magnitude. The analysis therefore focuses on how these parameters affect the absolute magnitude of the inferred effective grain-size proxy, D_{73}, and on whether the station-to-station pattern is preserved. The reference model uses $Q = 5$ and $v_{c0} = 800$ m s^{-1}, where v_{c0} is the reference Rayleigh-wave phase velocity at 1 Hz.

Sensitivity to seismic attenuation. Because attenuation exerts a first-order control on the coupling term, we tested the sensitivity of inferred D_{73} to a broader range of quality factors, $Q = 3, 5, 10$, while keeping the remaining reference parameters fixed. This range spans strongly attenuating near-surface channel conditions and broader values commonly used when site-specific attenuation measurements are unavailable.

Changing Q substantially rescales the inferred D_{73} values without changing the spatial pattern across the network (Supplementary Fig. S4a). Relative to the reference case ($Q = 5$), the tested attenuation range produces large changes in the absolute magnitude of peak D_{73} at all stations. For example, D_{73} at FGL1 varies from 0.37 to 2.07 m around a reference value of 1.00 m, whereas at FGL9 it varies from 0.13 to 0.73 m around a reference value of 0.35 m. Using the FGL6 reference value of 0.46 m, the corresponding range is 0.17–0.95 m. This confirms that the inversion should be interpreted primarily in terms of relative spatial patterns and order-of-magnitude effective particle-size estimates, rather than as an absolute grain-size measurement. However, the station-to-station pattern is preserved across all tested Q values: upper-reach stations retain higher effective D_{73} values than lower-reach stations, and the downstream reduction in effective coarse-particle diameter remains robust.

Sensitivity to the seismic velocity model. We also tested the effect of the reference Rayleigh-wave phase velocity v_{c0} on the inversion. The parameter v_{c0} was varied between 400 and 1200 m s^{-1}, corresponding to a $\pm 50\%$ perturbation around the reference value of 800 m s^{-1}, while keeping $Q = 5$ fixed. This range was used as a conservative sensitivity test for poorly constrained near-surface velocity structure in volcaniclastic channel deposits.

The effect of v_{c0} is much smaller than that of attenuation (Supplementary Fig. S4b). Across all stations, varying v_{c0} between 400 and 1200 m s^{-1} changes peak D_{73} by approximately -7% to $+6\%$ relative to the reference model. For example, D_{73} at FGL1 varies from 0.93 to 1.06 m around a reference value of 1.00 m, and at FGL9 from 0.33 to 0.37 m around a reference value of 0.35 m. For FGL6 the corresponding range is 0.43–0.48 m. The station-to-station pattern and the upper- to lower-reach contrast remain unchanged across the tested velocity range.

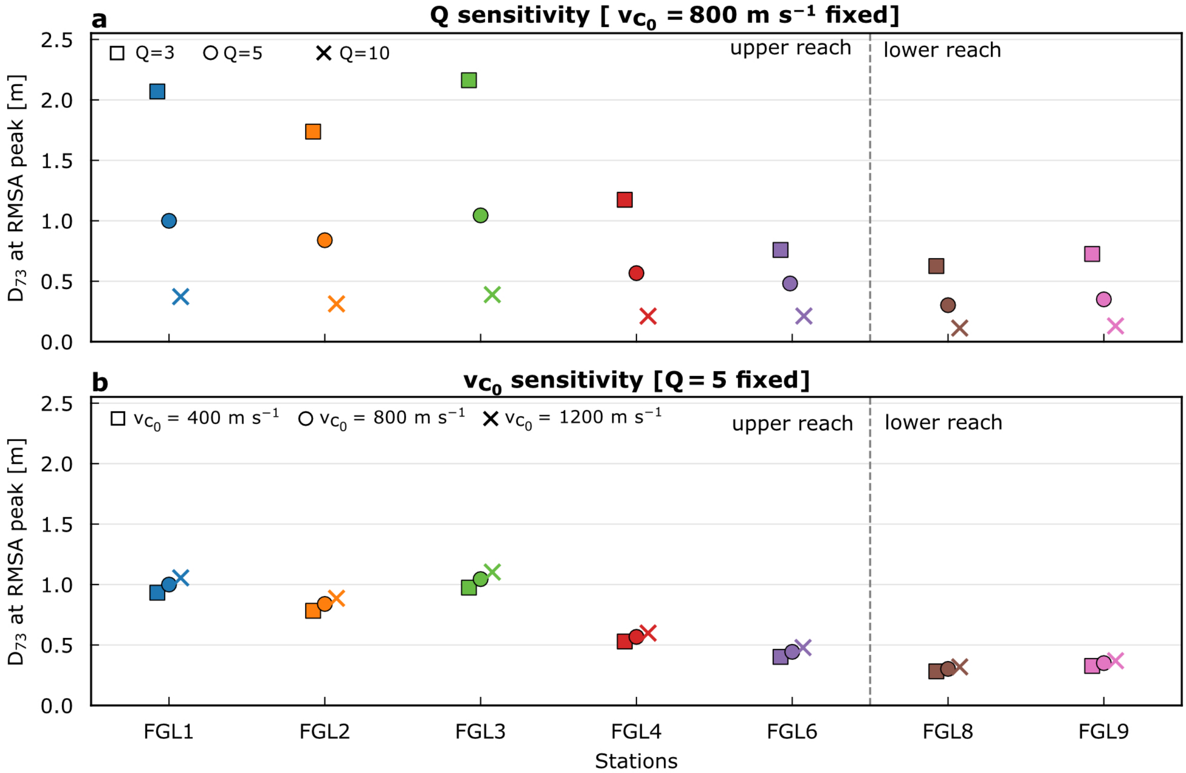

Supplementary Fig. S4: **Sensitivity of the thin-flow inversion to seismic attenuation and velocity structure.** **a**, Effect of varying the quality factor Q between 3, 5 and 10 while keeping the reference Rayleigh-wave phase velocity fixed at $v_{c0} = 800$ m s^{-1}. The reference model is $Q = 5$. Lower Q values increase the inferred D_{73}, whereas higher Q values decrease it. **b**, Effect of varying v_{c0} between 400, 800 and 1200 m s^{-1} while keeping $Q = 5$ fixed. The reference model is $v_{c0} = 800$ m s^{-1}. Variations in v_{c0} produce smaller changes than variations in Q. In both tests, the station-to-station pattern and the contrast between upper- and lower-reach stations are preserved. The dashed vertical line separates the upper and lower reaches.

References

[1] Gheri, D., De Angelis, S., Pineda, A., Woodhouse, M. & Phillips, J. Seismo-acoustic observations and video records of a lahar at volcán de fuego, guatemala (2026).

[2] Gheri, D., De Angelis, S., Pineda, A., Woodhouse, M. & Phillips, J. A high-resolution seismo-acoustic and video dataset of a lahar at volcán de fuego, guatemala. *Scientific Data* **-**, – (2026).

[3] Mock, J. C., Johnson, J. B., Pineda, A., Bejar, G. & Roca, A. Uav-based quantification of dynamic lahar channel morphology at volcán de fuego, guatemala. *Remote Sensing* **15**, 3713 (2023).

[4] Patalano, A., García, C. M. & Rodríguez, A. Rectification of image velocity results (river): A simple and user-friendly toolbox for large scale water surface particle image velocimetry (piv) and particle tracking velocimetry (ptv). *Computers & Geosciences* **109**, 323–330 (2017).

[5] Tsai, V. C., Minchew, B., Lamb, M. P. & Ampuero, J.-P. A physical model for seismic noise generation from sediment transport in rivers. *Geophysical Research Letters* **39** (2012).

[6] Farin, M., Tsai, V. C., Lamb, M. P. & Allstadt, K. E. A physical model of the high-frequency seismic signal generated by debris flows. *Earth Surface Processes and Landforms* **44**, 2529–2543 (2019).

[7] Perrier, L., Métaxian, J.-P., Battaglia, J. & Garaebiti, E. Estimation of the near-surface velocity structure of the yasur-yenkahe volcanic complex, vanuatu. *Journal of volcanology and geothermal research* **227**, 50–60 (2012).

[8] Moscatelli, M. *et al.* Physical stratigraphy and geotechnical properties controlling the local seismic response in explosive volcanic settings: the stracciacappa maar (central italy). *Bulletin of Engineering Geology and the Environment* **80**, 179–199 (2021).

[9] De Landro, G. *et al.* High resolution attenuation images from active seismic data: The case study of solfatara volcano (southern italy). *Frontiers in Earth Science* **7**, 295 (2019).

[10] Conner, A. E. *et al.* Quantifying seismic properties of a river channel at mount rainier for use in debris flow monitoring and analysis. *Seismological Research Letters* (2026).